This is the Author's [*accepted*] manuscript version of the following contribution:

[Junkai Ren, Luigi Stagi, Luca Malfatti, Carlo Maria Carbonaro, Gaetano Granozzi, Laura Calvillo, Sebastiano Garroni, Stefano Enzo, Plinio Innocenzi, Engineering UV-emitting defects in h-BN nanodots by a top-down route, Applied Surface Science, 567, 2021, 150727]

The publisher's version is available at:

https://doi.org/10.1016/j.apsusc.2021.150727

When citing, please refer to the published version.

Engineering UV-emitting defects in h-BN nanodots by a top-down route

Junkai Ren [a], Luigi Stagi [a,*], Luca Malfatti [a], Carlo Maria Carbonaro [b], Gaetano Granozzi [c], Laura Calvillo [c], Sebastiano Garroni[a] , Stefano Enzo [a], and Plinio Innocenzi [a,*]

[a] Department of Chemistry and Pharmacy, Laboratory of Materials Science and Nanotechnology, CR-INSTM, University of Sassari, Via Vienna 2, 07100, Sassari, Italy
[b] Department of Physics, University of Cagliari, sp 8, km 0.700, 09042, Monserrato, Italy
[c] Department of Chemical Sciences, University of Padua, Via Marzolo 1, 35131 Padova, Italy

*Corresponding authors: lstagi@uniss.it, plinio@uniss.it

Graphical abstract
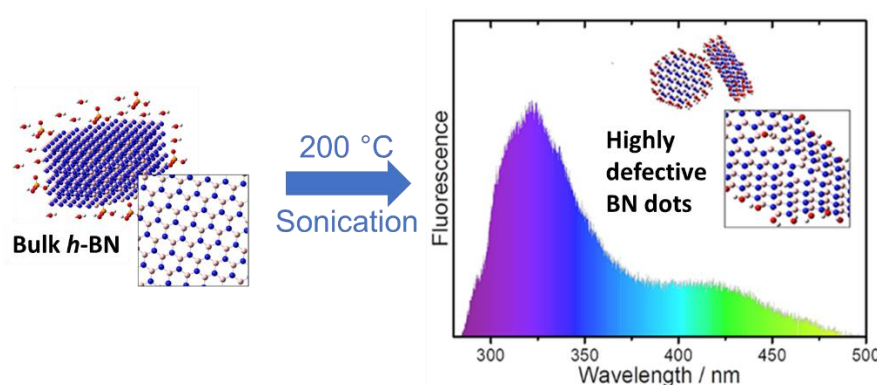
Abstract

Hexagonal boron nitride (*h*-BN) nanodots of 10 nm have been synthesized via top-down route from bulk powders. A combination of ultrasonic and thermal treatments in phosphoric acid has been used to achieve edge etching and size reduction to the nanoscale. A new emission in the ultraviolet region, correlated to a characteristic infrared-active vibration, has been detected in the BN dots. The UV emission is stable in as-prepared samples but quenches after thermal treatments higher than 100°C. Besides the UV band, the fluorescent emission of *h*-BN shows a broad band in the visible region, whose intensity reaches a maximum after thermal treatment at 200 °C. Structural and optical characterization techniques have been used to investigate the synthesis-properties relationship in *h*-BN and the hydroxyl covalent functionalization of the surfaces. The experiments show that the particular combination of ultrasonic treatment and etching in temperature is essential to achieve the UV fluorescent emission. Quantum chemistry calculations have been used to evaluate Stones-Wales defects as possible causes of the optical and vibrational properties.

Keywords: Boron Nitride, Photoluminescence, Nanodots

1. Introduction

Bidimensional hexagonal boron nitride (*h*-BN) represents one of the most interesting layered materials whose properties are expected to have a significant impact on electronics and

optoelectronics [1]. *h*-BN has a wide bandgap, around 6 eV [2], and localized defects with single-photon emission properties, making it an exciting material in photonics [3, 4]. 2D *h*-BN is also called "white graphene" due to its structural analogy to graphene [5]. Similarly to graphene quantum dots (GQDs), *h*-BN dots (BNDs) have been also fabricated and show a remarkable visible fluorescence, high dispersibility, and biocompatibility, which make them suitable for bioimaging applications [6]. The luminescent mechanisms of BN nanodots are usually attributed to radiative recombinations in boron/nitrogen vacancies, carbene structure, and oxygen-doping [7, 8].

The growing interest in BNDs has brought to the development of several synthesis strategies. By controlling the processing parameters, different systems with a large variety of properties are obtained [7]. BNDs can be synthesized using bottom-up and top-down routes and different precursors such as H_3BO_3, NH_3, $C_3H_6N_6$, $CH_3CH_2NH_2$ have been employed in the preparation of BNDs via hydrothermal or solvothermal methods [9-11]. In a previous work [12], BNDs have been produced via a bottom-up route using a simple hydrothermal processing of a H_3BO_3 - NH_3 mixture. The final products were boron-oxynitride dots with two color emissions in the blue and in the green [12]. In general, it has been observed that bottom-up routes do not allow obtaining pure BN dots, and impurities such as oxygen and carbon can be incorporated in the structure affecting the material properties.

An alternative is the production of BNDs via top-down processing where bulk *h*-BN powders are exfoliated and shattered by cavitation procedure. Among the others, sonication, ball-milling, solvothermal or microwave treatments in a variety of different solvents have been used to prepare BNDs. Water, ethylene glycol, dimethylformamide (DMF) and 1-metil-2-pyrrolidone (NMP) are among the most used solvents [13-16]. Because of the organic solvents, carbon, oxygen and hydrogen impurities generally enter into the B-N structure of the dots. The presence of carbon atoms is a source of uncertainty in modulating and understanding the optical and structural properties of *h*-BN systems [17, 18]. However, to avoid the uncontrolled introduction of carbon, a carbon-free liquid phase can be selected to assist the exfoliation of BN bulk materials [8].

In general, BNDs exhibit a blue emission under UV irradiation and can be easily dispersed in water. Although the origin of blue fluorescence is frequently attributed to both oxygen and carbon impurities, a convincing attribution is still lacking. Another important role is played by hydroxyl -OH groups, which are structural defects which cannot be ruled out, especially as edge defects [19, 20]. Although high oxidative environment, such as acid, weakly affects the amount of -OH groups at the edges due to the high hydrophobicity of *h*-BN,[21] it has been reported that di-tert-butylperoxide (TBP) can oxidize the *h*-BN surfaces if combined with sulfuric acid in a two-step method [21].

Despite the great efforts in engineering the BN-based systems, the fabrication of BNDs with controlled properties in terms of dimension, shape, structure, and functional response is a highly challenging task. Controlling composition and defects is mandatory because of the considerable impact on optical properties. A top-down approach has the advantage to start from a bulk BN material of defined composition, but also in this case formation of defects should be expected. In the present work, we have developed a two-step procedure to obtain UV and visible emitting BNDs by heating bulk *h*-BN in H_3PO_4 and treating the resulting product in an ultrasonic bath for several hours. The synthesized BNDs present common structural features

with bulk *h*-BN but display new optical and vibrational properties that are strictly connected.

2. Results and discussion

2.1. Morphology and structure

We have used a combination of ultrasonication and thermal treatment in H_3PO_4 to form *h*-BN nanodots. In the first step, *h*-BN powders have been dispersed in concentrated H_3PO_4 and thermally treated at 200 °C for 1 h. Then, the dispersion has been ultrasonicated for 15 h and larger *h*-BN particles have been removed by centrifugation. BNDs have been purified by dialysis and filtered. The BNDs powders have been dried before structural and optical characterizations. The characterizations have been also performed in samples treated at the temperature of 100, 200, and 300 °C.

The BNDs formation by etching has been confirmed by the morphological characterization performed by TEM **(Figure 1).** The dots (black dots in the image) appear of spherical shape and less than 10 nm in size.
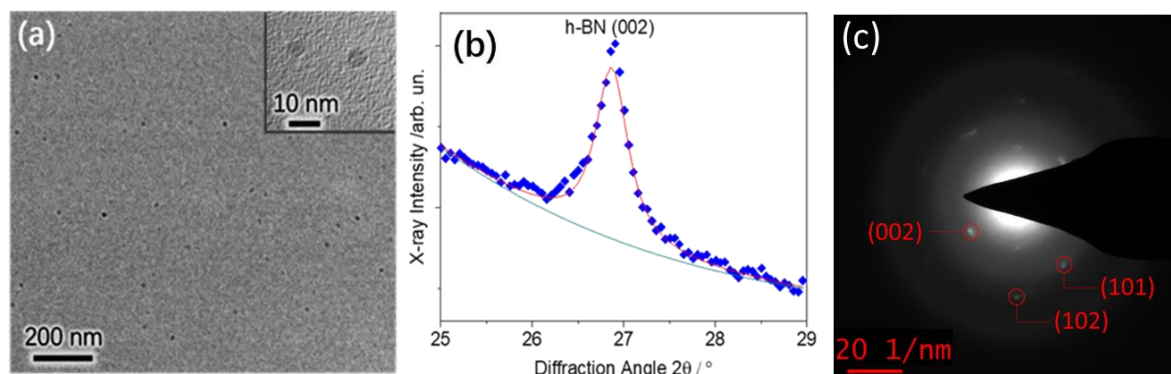

Figure 1. (a) TEM image of as-prepared BN dots. The inset shows a TEM enlarged region. (b) Diffraction pattern of BNDs. (c) Selected-area of an electron diffraction (SAED) pattern.

The inset in the **Figure 1a** shows an enlarged area with two BN dots; the low contrast generated by the low-density BNDs with respect to the grid material has not allowed capturing further details of the structural conditions of edges or planes. In other terms, the images do not allow getting a better insight about the efficacy of the exfoliation process. To investigate the effect of the synthesis and heating in air on BNDs structures, we have employed Raman spectroscopy, an effective technique to evaluate the exfoliation degree of layered nanostructures [22, 23]. Bulk *h*-BN exhibits the characteristic E_{2g} phonon mode at ~1366.5 cm^{-1}, which is affected by a remarkable shift toward higher wavenumbers as the number of layers in stacked hexagonal structure approaches the monolayer condition [22]. As reported in **Figure 2**, the Raman signature of bulk crystal is well reproduced in the raw material. The as-prepared and thermally treated BNDs samples do not display a significant variance from the reference bulk value, indicating that the number of BNDs layers is greater than 10 [22]. **Figure S1** shows a representative AFM image of the BNDs; the dimensions do not exceed 15 nm in height confirming the presence of an unexfoliated layered structure, in accordance with Raman results. X-ray diffraction pattern confirms the hexagonal stacked structure of BNDs, showing the characteristic peak at 26.8° that corresponds to (002) planes (**Figure 1b**) [24].
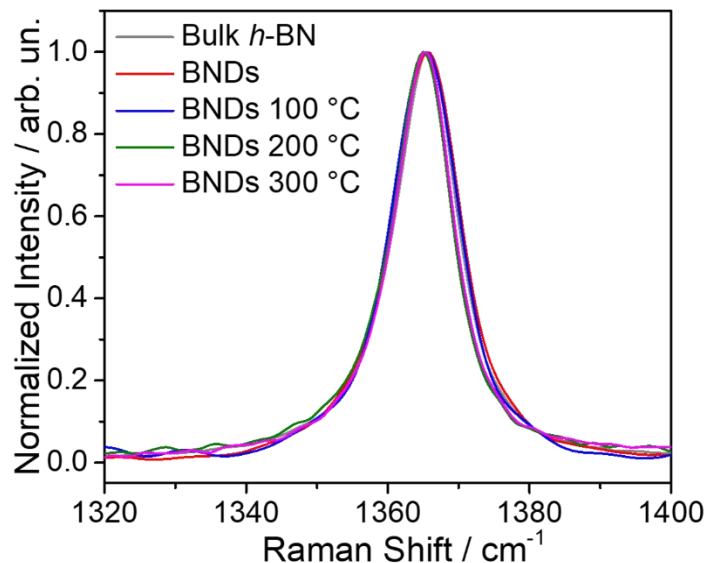
Figure 2. Raman spectra of bulk *h*-BN, as-prepared BNDs and thermally treated dots at different temperatures collected between 1320 – 1400 cm^{-1}.

2.2. Optical properties

Figure 3 shows the 3D excitation-emission-intensity spectra and the corresponding PL spectra of BNDs in the range between 200 and 600 nm; the emission spectra have been acquired using BNDs dispersions in water. The spectra show the fluorescence response of as-prepared BNDs and BNDs treated at 100, 200, and 300 °C in air. This analysis has been done to evaluate the different emissions after a thermal treatment in oxidizing conditions. Two well-defined emissions are observed in pristine BNDs as the excitation wavelength changes in the range of 250 – 400 nm. The first emission rises in the ultraviolet region from 300 to 370 nm under excitation at 270 nm. The second band extends from 370 to 530 nm, with the excitation and emission maxima at 310 and 420 nm, respectively. The blue emission can also be excited under 270 nm irradiation, which, in turn, generates a characteristic UV-blue double fluorescence **(Figure 3e)**. The corresponding absolute QYs of the two emissions under excitation at 270 and 310 nm is 1.4 and 1.5 %, respectively.

Interestingly, the UV emission can only be detected after both heating and sonication in acid, whilst is not observed if the *h*-BN powders are only subjected to either heat treatment or sonication **(Figure S2)**. The visible emission has been already observed in many *h*-BN exfoliated systems, especially in those making use of water or oxidizers as exfoliating agents. In our previous work [8], we have demonstrated the correlation of blue emitters defects with hydroxyl groups in water-exfoliated *h*-BN nanosheets. These defects are optically active at room temperature and witness a remarkable enhancement at the temperature of 300 °C. At higher temperatures, the PL emission strongly decreases as a result of the oxidation process which gives a boroxyl-like structure [8].

Moreover, the recombination lifetime is typically unaffected by thermal treatment. This is confirmed in BNDs **(Figure 4** and **Table S1)** where the thermal treatments of BNDs up to 200 °C cause a strong fluorescent quenching of the emission centered at 325 nm and an enhancement of luminescence located at 420 nm. The blue emission reaches a maximum at 200 °C in perfect accordance with our previous findings. The average recombination lifetimes

are calculated to be around 3.7 – 3.8 ns. In a recent article [25], a broad fluorescence with a maximum at 3.9 eV has also been observed in polycrystalline BN. Besides, another sharper emission at high energy (~5.5 eV) has been also revealed but it has been attributed to carbon impurities. The broad emission is detectable at room temperature and it is assigned to donor-acceptor pairs of localized centers in correspondence of defects strongly coupled to the lattice [25]. These defects could be originated by boron or nitrogen vacancies (V_B or V_N) or their coupling with oxygen impurities (V_B-O_N). Similarly, an emission around 4 eV has been observed in boron nitride grown by high temperature molecular beam epitaxy (MBE) [26]. Stone–Wales defects, generated by rotating a B-N pair by 90°, are also considered a possible source of UV emissions [27]. The photoluminescence triggered at 260 nm originates from particular structural defects that may be present in the crystal lattice of boron nitride irrespective of the particular morphology. There is a peculiar correlation between fluorescence and structural properties as will be evident from the infrared absorption spectra (*vide infra*).
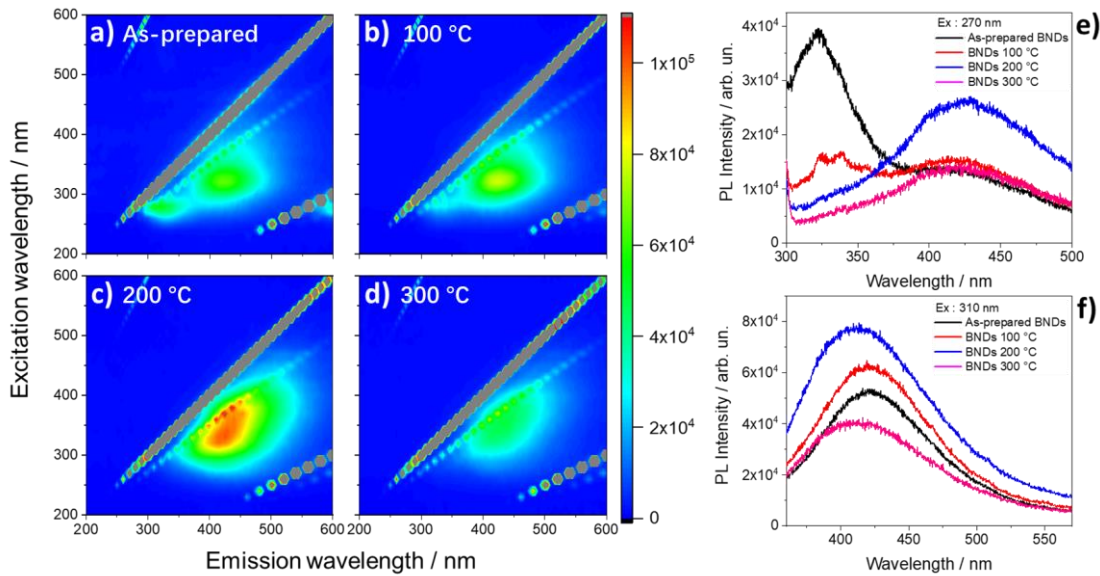

Figure 3. (a-d) 3D PL excitation (y-axis)-emission (x-axis)-intensity spectra in the 200-600 nm ranges of as-prepared BN dots and thermally treated dots at different temperatures. The intensity is shown as a false color scale. The grey regions are caused by excitation first and second orders. (e-f) 2D PL spectra of as-prepared BN dots and thermally treated dots at different temperatures, under the excitation wavelengths of (e) 270 nm, and (f) 310 nm.
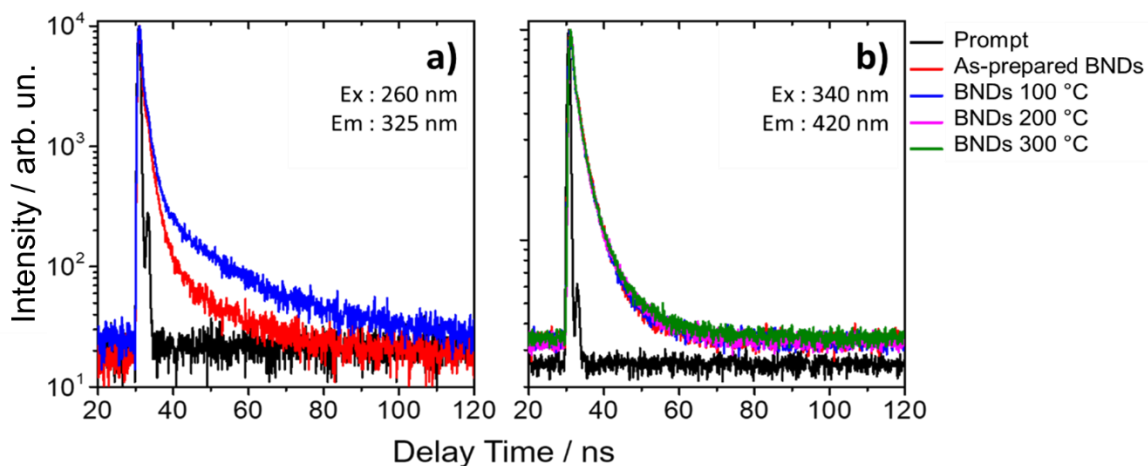
Figure 4. Fluorescence lifetime curves of the as-prepared BN dots and thermally treated dots at different temperatures. (a) λ_{ex} = 260 nm, and λ_{em} = 325 nm; (b) λ_{ex} = 340 nm, and λ_{ex} = 420 nm.

Figure 5 shows the UV-Vis absorption spectra of the pristine and thermally treated BNDs at 100, 200, and 300 °C, respectively. The spectra have been acquired in an aqueous solution at the concentration of 10 µg mL^{-1}. BNDs show an intense deep UV absorption band with a broad absorption tail that becomes more intense in the 200 and 300 °C samples. The absorption extends in the visible range in the high temperature treated samples. High energy absorption (~6 eV) is attributed to the band-to-band transition of the intrinsic h-BN [28]. The plot shows a drop of absorption at around 200 nm in the 100 and 200°C treated samples. We have not observed any change in the dispersibility of BNDs as an effect of possible modification in the surface hydrophilicity [21]. In fact, the solutions remain stable with time, and we can reasonably attribute the UV-Vis variation to a significant alteration of the intrinsic BNDs structural properties. The inset of **Figure 5** shows an enlarged region of the UV-Vis spectra which has been used to calculate the BN dots energy gap (E_g) by the Tauc method [29]. The E_g of the as-prepared BNDs is around 5.47 eV and shifts to higher values as a function of the thermal treatment (5.58 eV at 100°C, 5.69 eV at 200°C, and 5.80 eV at 300°C). Intragap absorption of a distribution of defects typically arises as a tail in the proximity of bandgap transitions in h-BN. As an effect of annealing and reduced structural disorder, a shift of the absorption edge towards higher energies is observed, as already reported in metal-organic chemical vapor deposition (MOCVD) h-BN films [30]. In contrast, the rise of absorption bands at higher wavelengths after annealing > 100 °C is attributed to the oxidation of persistent defects in the h-BN structure during the thermal treatment in air [31].
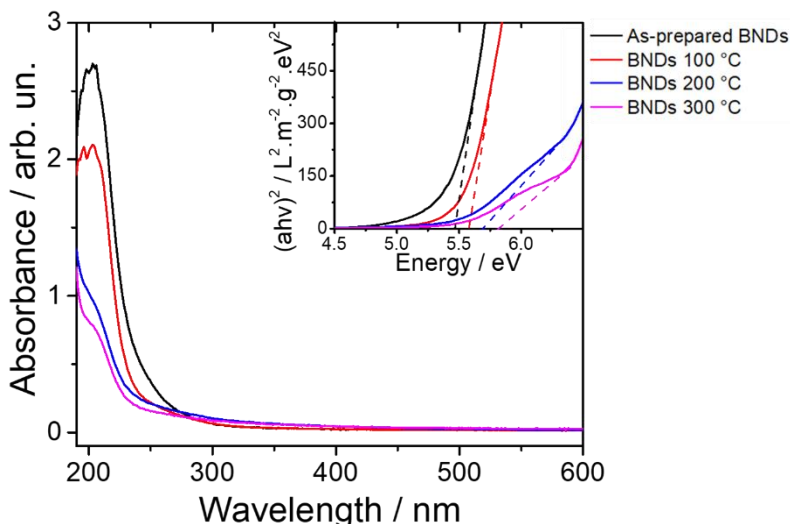
Figure 5. UV-Vis absorption spectra the as-prepared BN dots and after thermal treatment at different temperatures. Inset shows an enlarged region of absorption spectra.

2.3. Chemical composition

Fourier-transform infrared spectroscopy (FTIR) analysis has been used to identify the surface functional groups and investigating the potential effects of the synthesis on the *h*-BN structure. The results are summarized in **Figure 6**. Bulk *h*-BN exhibits two characteristic vibrational modes at 1371 (E_{1u}) and 819 cm^{-1} (A_{2u}), which represent the in-plane B-N transverse stretching vibration and the out-of-plane B-N-B bending mode, respectively [8, 12, 32]. Compared with bulk data, the two characteristic bands at about 1372 and 818 cm^{-1} of the nano-sized BN show a narrower FWHM. Although it has been ignored in many published articles, this phenomenon can be frequently encountered in reported infrared data of BN materials, including both 2D nanosheets [33-35] and 0D nanodots [14, 15, 36, 37]. We do not specifically address the problem in this work, but it is reasonable to suppose that the decrease of dimensions and edge effects can bear on the B-N bonds and the related vibrational modes distribution. Correspondingly, the intensity ratio of the two bands in BN dots (I_{1372}: I_{818}, 5.068) is much larger than that in bulk *h*-BN (I_{1372}: I_{818}, 3.067), which is likely correlated with modification in interplanar interactions.

Besides the most intense vibrations, BNDs infrared spectra are characterized by several well-defined modes in the 850 – 1300 and 400 – 700 cm^{-1} regions. The latter range can be used to detect the BN structure oxidation and the creation of characteristic B-O and B-OH bonds [8]. To study the first region, we have compared the BNDs infrared spectra with those of an H$_3$PO$_4$ solution shown in **Figure S3** as a reference. In H$_3$PO$_4$, we have identified the characteristic P-OH stretching vibration at around 970 cm^{-1} as the most intense contribution [38]. The less sharp absorptions at higher wavenumbers can be attributed to PO-H bending (1111 cm^{-1}) and P=O stretching (1212 cm^{-1}) [39]. The infrared spectra collected in previous experiments about the use of H$_3$PO$_4$ in exfoliation and treatment of BN, show vibrations at 1080 and 1025 cm^{-1} attributed to P-O-C and POH groups [40, 41]. Although we can exclude the contribution from carbons, the infrared modes at 926 and 1086 cm^{-1} in BNDs could be attributed to the possible presence of intercalated acid. However, no H$_3$PO$_4$ Raman fingerprints are detected as it should be in the acid-treated BN samples [41]. In light of this, it is more reasonable to attribute the bands between 900 and 1100 cm^{-1} to B-O stretching, as already observed on oxidized *h*-BN
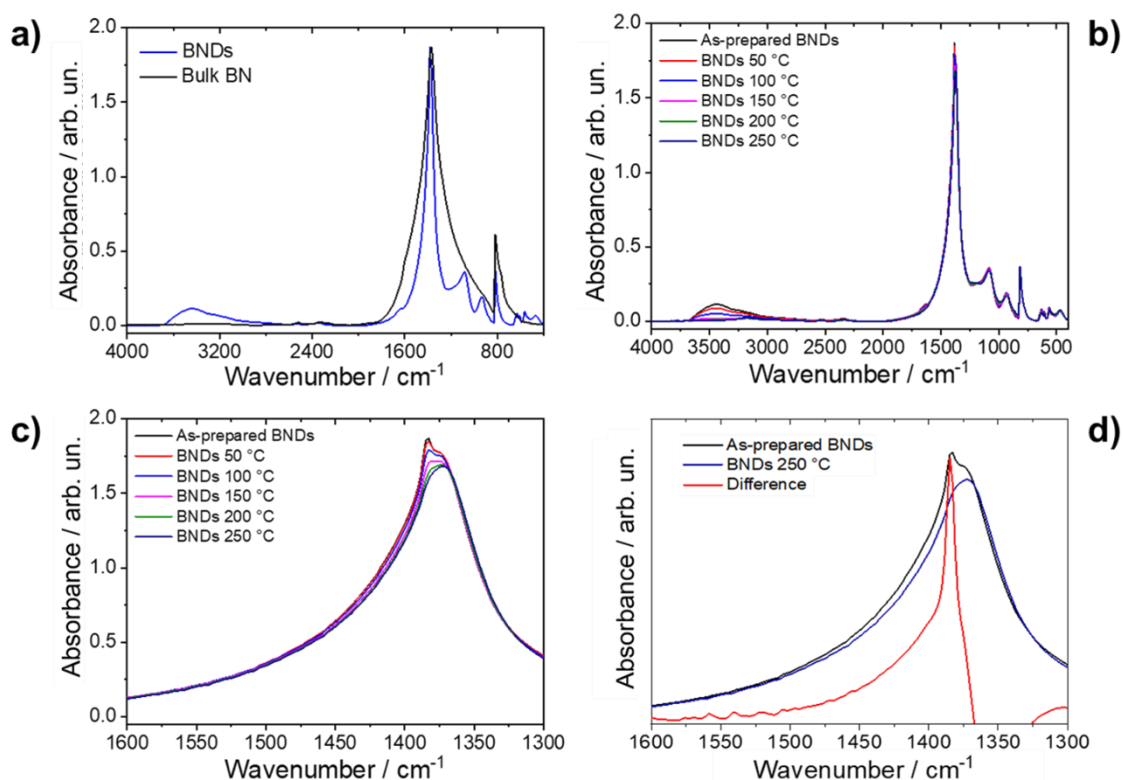
nanosheets [42].

Figure 6. (a) FTIR spectra of bulk h-BN powder (black curve) and BNDs (blue curve). In situ FTIR spectra as a function of temperature at (b) 1300-1600 cm^{-1} and (c) 2400-2600 cm^{-1}. (d) The spectral difference between as-prepared BNDs and the dots treated at 250 °C.

Figure 6c shows the FTIR spectra with the characteristic in-plane B-N stretching at 1372 cm^{-1}. The band appears formed by two overlapping components, an almost temperature-independent mode at 1372 cm^{-1} and a second band around 1383 cm^{-1}. The latter monotonically decreases with the temperature and vanishes at 250 °C. The spectral difference between the as-prepared BNDs and the 250 °C dots points out the presence of a sharp mode with a maximum at 1385 cm^{-1} (**Figure 6d**). Importantly, this vibration is correlated to the UV emission at 320 nm for as much as the annealing promotes a decrease of both high energy fluorescence and infrared absorption. This allows us to make a direct correspondence between these two BNDs physical properties.

As far as we know, the split of E_{1u} has been only observed in a few articles. For example, a marked split has been observed in BN nanodots synthesized by exfoliation and cracking of BN sheets through heating with potassium and reaction with an EtOH/water solution. The method has been affected by a high percentage of carbon contamination, whose major contributions arose at 1500 – 1650 cm^{-1} [43]. Similarly, two vibrations at 1385 and 1439 cm^{-1} have been observed in BN dots obtained by hydrothermal method from boric acid/urea reaction and attributed to edge oxidation [44]. High-temperature treatment of ferrite nanoparticles and h-BN followed by water vapor exposure has proved to induce extensive physical defects which can be easily saturated by OH- groups. The resulting edge-hydroxylated BN dots display a sharp absorption at about 1400 cm^{-1}. After hydroxylation, two fluorescent emissions are

detected at around 330 and 440 nm [45]. These findings allow excluding carbon contaminants and functionalization with PO groups as causes of BNDs optical and vibrational properties.

The splitting in the 1300 – 1600 cm^{-1} infrared region primarily involves B-N stretching and the intrinsic hexagonal crystal structure. We presume that a characteristic defect and the consequent local deformation of the lattice can affect the BN in-plane vibrational features. This defect is at the origin of the UV fluorescent emission and is associated with saturating -OH and -H groups. DFT calculations report that pentagon–heptagon Stone–Wales (SW) defects with optical transition at around 4 eV can arise because of the favorable energetic conditions of large strain at the grain boundaries [27]. Two weaker vibrations are identified at 2425 and 2525 cm^{-1}, which are assigned to B-H stretching mode. Although the higher wavenumbers vibration is not affected by the temperature, the 2425 cm^{-1} mode decreases in the investigated thermal range.

Figure S4 shows a detailed study of O-H and N-H stretching bands by *in-situ* IR measurement in the 3800 – 2600 cm^{-1} range. The spectra have been deconvoluted into three components by a Gaussian model. The deconvoluted bands at 3448 and 2896 cm^{-1} are assigned to hydrogen-bonded O-H and O-H adsorbed at the surfaces. The thermal treatment leads to a rapid decrease of the high frequency component and a relatively slower decline of the lower one. It also suggests that the B-OH groups are mostly in isolated state after higher temperature process. The middle deconvoluted peak at 3181 cm^{-1} is caused by the N-H stretch absorption. The infrared N-H in intensity shows a trend similar to the B-OH component. Upon annealing to 200 and 250 °C, the spectra show minor changes.

Figure 7 shows the differential thermal analysis - thermogravimetric analysis (DTA-TGA) data. These results, coupled with *in-situ* FTIR data in **Figure S4**, are helpful to understand the possible structural change of the as-prepared BN dots as a function of the temperature. Two endothermic events have been observed: (i) in the range between 25 and 90 °C, a relative minimum is observed at 42 °C, corresponding to a 9.4% weigh loss due to molecular desorption of water in BN products; (ii) in the range between 90 and 300 °C, the second minimum at 180 °C, with a broad structure at 215 °C, is attributed to a progressive condensation of B-OH and formation of N-B-O structure determining a 16.2% of weigh losses. Moreover, for the temperature higher than 300 °C, the strong oxidation further leads to boroxyl rings structures [8].
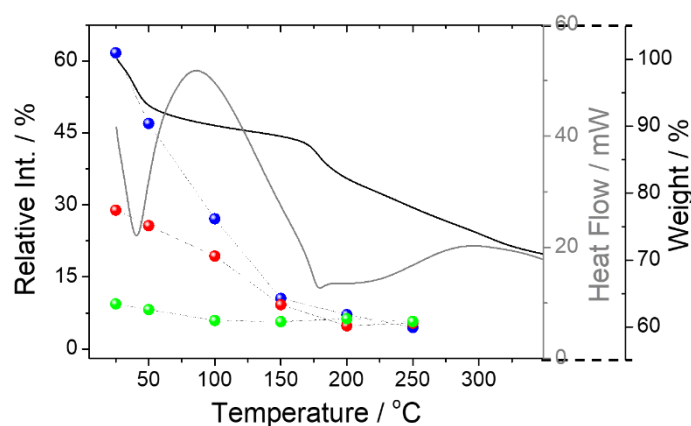

Figure 7. TGA-DTA of the as-prepared BN dots, with the relative absorption intensities of B-OH and N-H (blue, red, green dots, respectively) from FTIR spectra.

X-ray photoelectron spectroscopy (XPS) has been used to investigate possible variations of

stoichiometry and oxidation state of BNDs as a function of heating treatment. **Figure 8** shows the typical B 1s and N 1s peaks of BN structure before and after thermal treatments. **Table S2** summarizes the data analysis of both regions. In as-prepared BNDs, the main component is associated with conjugated boron-nitrogen bond at ~190.2 eV and ~397.6 eV, labeled as B-N and N-B, respectively [43, 46]. The middle components at ~191.3 and ~399.2 eV are identified with the existence of native oxides in BN structure, which are marked as B-(N,O) and N-(B,O) [12, 47]. As the temperature rises, a corresponding increase of both B-(N,O) and N-(B,O) species by thermal oxidation in air is observed; these data are in agreement with the change of the 1240 cm^{-1} infrared band as a function of the thermal treatment temperature. Two additional components are observed at ~193.4 and ~400.5 eV and attributed to B-O and N-H groups, respectively [9, 48]. Higher temperatures can cause an increase of B-O contribution due to the oxidized formation of boroxyl rings, which has also been confirmed by the 475 cm^{-1} IR band; on the other hand, it leads to an increase of N-H characteristic band, consistent with the 3200 cm^{-1} infrared band.
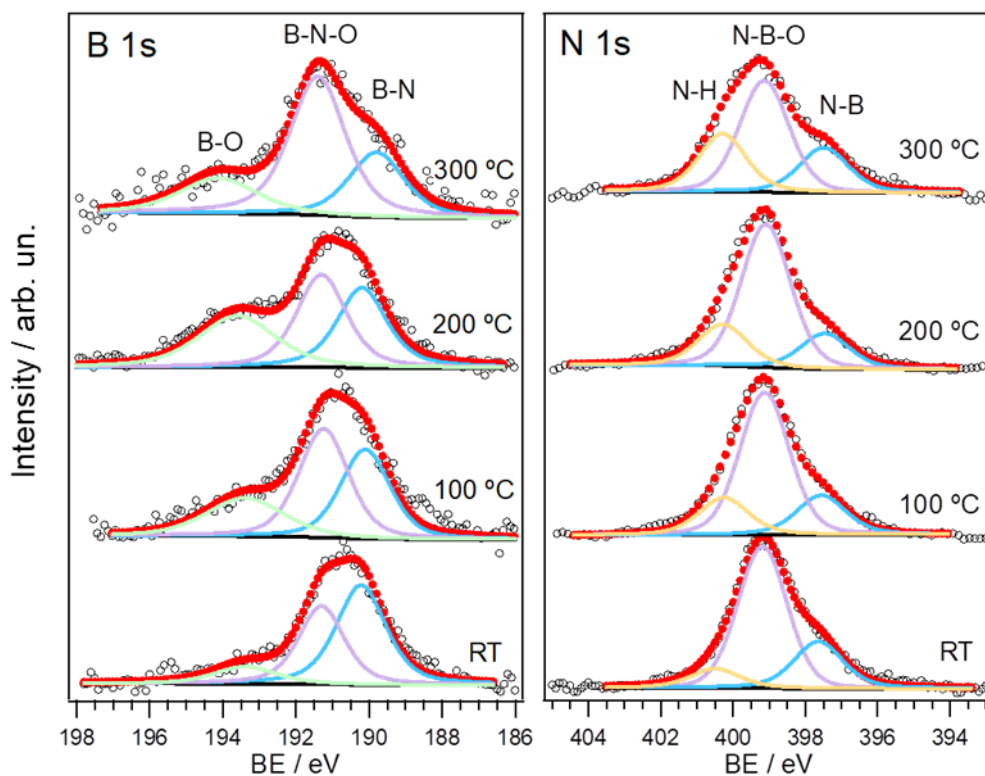

Figure 8. High-resolution B 1s and N 1s XPS spectra, and their corresponding deconvolution into chemically shifted components, for the pristine BN dots and after thermal treatment at 100, 200 and 300 °C.

2.4. Quantum chemical calculations

We have theoretically evaluated the effect of Stone Walls (SW)-defects on the structural and optical properties of a *h*-BN cluster system, as depicted in **Figure 9**. In this simplified model, we have built a hexagonal shaped monolayer of BN consisting of 61 rings and saturated edges with protons for a total of 180 atoms. The defective structure has been created by inserting a pentagon-heptagon as a consequence of a B-N couple rotation. This results in B-B and N-N couples keeping constant the sum of atoms in the cluster. The defects have been calculated in neutral charge configuration and the formation energy according to the following equation [8,

49] :

$$E_{form} = E_D(q) - E_{BN} + n_i\mu_i + q(E_{VBM} + E_F) \qquad (1)$$

where $E_D(q)$ is the defective structure energy with charge state q, E_{BN} is the non-defective cluster energy, n_i is the number of exchange species and μ_i is the chemical potential. E_{VBM} is the energy of the maximum of the valence band and E_F is the Fermi level. With the assumption ($q = 0$), the formula reduces into the difference of the two clusters formation energies. The defect-free cluster displays an intense optical absorption at 205 nm in good accordance with the experimental bulk value (5.95 – 6 eV) [2, 50]. The optimized structure shows a B-N bond length of 1.446 Å at the center and 1.419 Å at the edge, which are conform to the data reported for smaller clusters [8].

To investigate the impact of SW-defect on the cluster optical absorption, we have introduced the characteristic pentagon–heptagon geometry in the core of the structure and let it to relax into the lower energy configuration. In addition to single defect, the UV-Vis absorption has been calculated in presence of two and three SW-defects. As shown in **Figure 9a**, the SW-defect determines a low energy transition at 283 nm, which is mainly enhanced with two or three SW-defects (BN(2SW), 281 nm; BN(3SW), 273 nm). The stronger band-to-band transition redshifts in BN(SW) up to 227 nm. We attribute this effect to the defect-related structural deformation that bends the planar geometry of the BN cluster (**Figure 9b**). It is worth noting that the calculated optical features are in very good agreement with the experimental ones. Indeed, the presence of defects produces an absorption tail estimated at about 227 nm, as the calculated band-to-band transition in the defective BN(SW). In addition, the low energy transition of the BN(SW) system agrees very well with the excitation band of the UV emission recorded in the as-prepared BN samples (see **Figure 3**). The HOMO-LUMO transition in the defective BN(SW) system is depicted in **Figure 9a** along with the molecular orbital representation of the two states showing a strong localization of the charge distribution around the SW defect. The corresponding calculated infrared spectra are reported in **Figure 9c-d**. Although affected by our model limits (single layer, hydrogen saturation of edges and small dimension), the IR spectra present a good qualitative accordance with the experimental data. As the effect of SW-defect, we observe a remarkable modulation of in-plane BN bending that we attribute to the strong removal of BN planarity. Furthermore, we estimate the formation energy of SW-defect as a function of position in the cluster (**Figure S5**). By using the Eq.1, we have calculated a formation energy of 6.35 eV and 5.45 eV at the center (BN(SW)$_c$) and at the edge (BN(SW)$_e$), respectively. This indicates that it is more favorable to promote the creation of SW-defects at the edge of BND structures. Despite the overestimation of vibrational frequencies, the optical transitions fit well the trend observed in the experimental spectra, corroborating the hypothesis of localized SW structural defects as a source of UV BNDs properties.
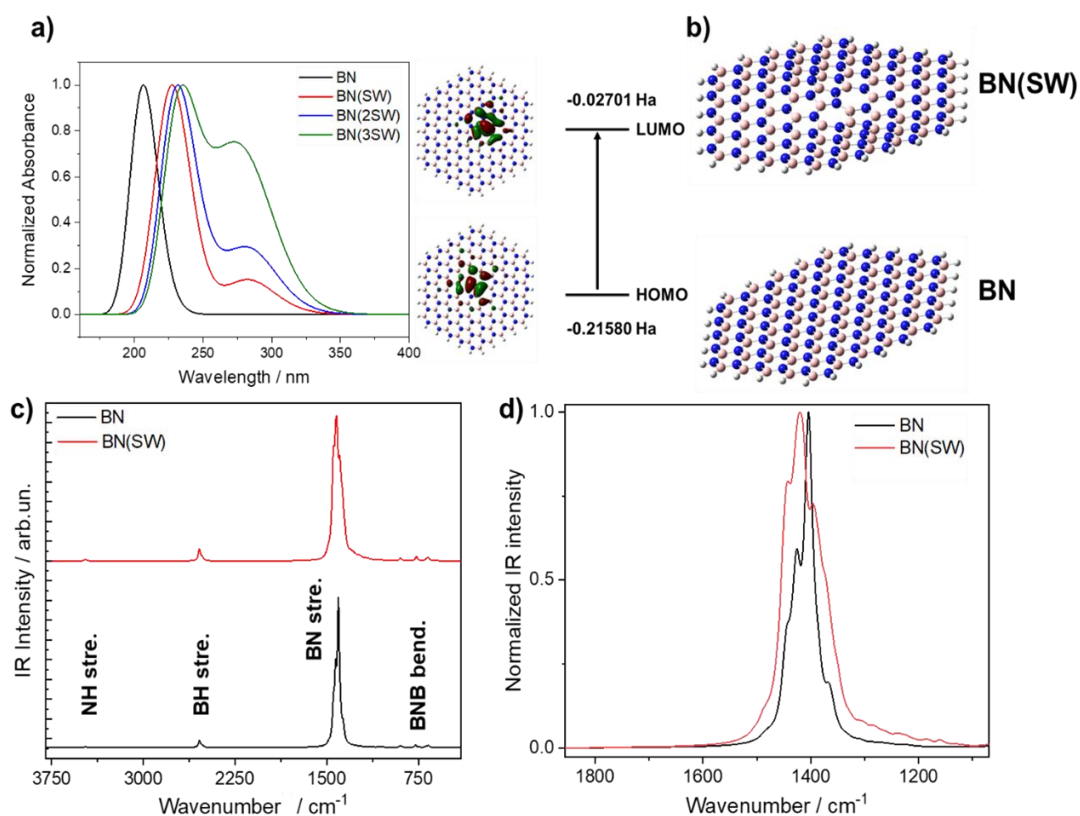
Figure 9. (a) Computed UV–Vis absorption of pristine (BN) and defective *h*-BN (BN(SW)) clusters and HOMO - LUMO representations of the computed defects. b) Representation of optimized BN and BN(SW) structures. c-d) Calculated infrared spectra of BN and BN(SW) clusters.

According to the experimental results herein reported, we have summarized the synthesis process and the effect of the Brønsted acid treatment in the **Scheme 1**. The *h*-BN bulk powders can be easily dispersed in a concentrated solution of orthophosphoric acid by fast sonication for a few minutes. The thermal treatment at 200 °C (close to the boiling point of ~212 °C), facilitates the intercalation and interaction of H_3PO_4 with the BN structure. The resulting strong oxidation leads to the breaking of B-N bonds, especially at the edges and exposed surfaces. The unsaturated bonds can work as anchor sites for -OH groups and protons. At the end of the process, the crystal structure appears highly defective as demonstrated by the emergence of UV emissions. The stressed and defective crystalline lattice can be further oxidized and strain-relaxed by high temperature annealing [51].
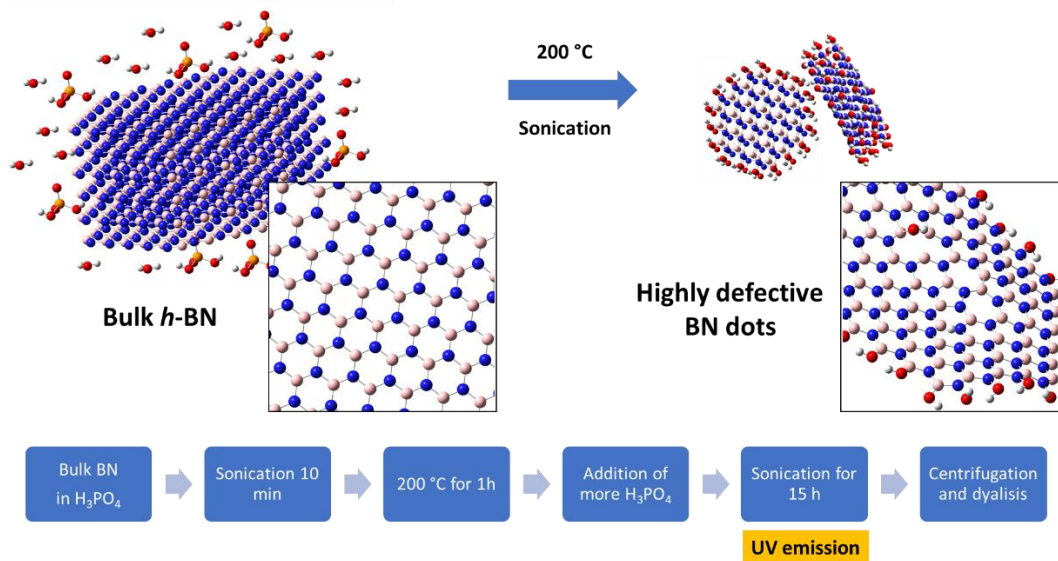
Scheme 1. Synthesis process of *h*-BN dots (BNDs) and defects induction mechanism. *h*-BN powders undergo to a strong oxidation by treatment at 200 °C and sonication for 15 h promoting structural cracking and decrease of the structural extension.

3. Conclusion

Defective hexagonal boron nitride nanodots (BNDs) have been synthesized using a top-down route by etching and oxidation of *h*-BN bulk powders in orthophosphoric acid. The resulting nanocrystals show two characteristic emissions in the UV and visible range. The visible fluorescence enhances with the temperature treatment up to 300 °C and it is related to the presence of hydroxyl groups as already observed in *h*-BN nanosheets. The photoluminescence at 325 nm quenches as a function of the thermal treatment temperature. Along with the UV fluorescence, a new sharp vibrational mode in the infrared spectra has been recognized; it disappears at 250 °C. This vibration has been attributed to a characteristic B-N stretching arising at the formation of UV-emitting defects. The new structural defects are stable at room temperature and are attributed to localized lattice deformations in presence of Stone-Wales defects.

4. Experimental Section

4.1. Chemicals

Hexagonal boron nitride powder (*h*-BN, 99.5%, Alfa Aesar) and orthophosphoric acid (H_3PO_4, 85%, Fluka) were used as received without further treatment.

4.2. Preparation of BN dots

Firstly, bulk *h*-BN (10 mg) powders were dispersed in H_3PO_4 (5 mL) in a glass vial (capacity 25 mL) by 10 min sonication. Then, the dispersions were thermally treated in air at 200 °C for 1 h. After cooling to 25°C, H_3PO_4 (15 mL) was added into the glass vial, which was immediately sealed. After 15 h sonication, the mixtures were centrifuged at 12000 rpm for 15 min to remove the unexfoliated and larger *h*-BNs. The supernatant containing BN dots was diluted by water, and purified using dialysis against water (2000 MWCO, Sigma-Aldrich) for 3 days. Finally, the BN dots aqueous solution was obtained by filtering through a 0.22 μm nylon membrane (Sigma-Aldrich). The product obtained by dialysis was finally dried in an

oven. Oxidation thermal treatments were carried out in air at different temperatures, 100, 200, and 300 °C.

4.3. Characterization methods

Transmission electron microscopy (TEM) images were acquired by a FEI Tecnai 200 microscope (Thermo Fisher Scientific) with a field emission gun operating at 200 kV.

X-ray diffraction (XRD) pattern was recorded by a high-resolution diffractometer (Rigaku SmartLab X-ray diffractometer equipped with a rotating anode 9kW) with a Cu Kα line (λ = 1.5406 Å) operating at 40 kV and 150 mA.

Raman measurements were performed by a "Senterra" Raman microscope (Bruker) under a laser excitation of 532 nm (1 mW power). The spectra were collected with a resolution of ~3 - 5 cm^{-1} and an integration time of 10 s.

Atomic Force Microscopy (AFM) were performed with a microscope NT-MDT Ntegra at 0.8 Hz scan speed in semicontact mode, using a silicon tip with nominal resonance frequency of 150 kHz, 5 N m^{-1} force constant, and 10 nm typical curvature radius.

Fourier-transform infrared spectroscopy (FTIR) analysis was done with an "infrared Vertex 70v" interferometer (Bruker) in transmission mode using a KBr pellet (IR 99%, Sigma). *In situ* FTIR spectra were collected in the range of 25 to 250 °C by an electrical heating jacket (Specac) with a temperature controller. The spectrum of H_3PO_4 solution was obtained by an attenuated total reflection (ATR) attachment (A225/Q Platinum, Bruker). The baselines were fitted by a concave rubber band correction with OPUS 7.0 software.

Thermal gravimetric analysis (TGA) was done from 25 to 800 °C with 5 °C min^{-1} of ramp rate under a nitrogen flow of 20 mL min^{-1} by an SDT-Q600 instrument (TA Instruments).

X-ray photoelectron spectroscopy (XPS) was carried out in a custom designed UHV system equipped with an EA 125 Omicron electron analyzer with five channeltrons, working at a base pressure of 10^{-10} mbar. Core level photoemission spectra (P 2p, B 1s, C 1s, N 1s and O 1s regions) were collected in normal emission at room temperature with a non-monochromatized Al K_α X-ray source (1486.7 eV) and using 0.1 eV steps, 0.5 s collection time and 20 eV pass energy.

UV-Vis absorption spectra were measured by a "Nicolet Evolution 300" UV-Vis spectrophotometer (Thermo Fisher) with a bandwidth of 1.5 nm.

Fluorescence spectra were recorded by a "Fluoromax-3" spectrofluorometer (Horiba Jobin Yvon) with a 3 nm slit for excitation and emission.

Absolute quantum yields (QYs) were calculated using a quanta-ϕ integrating sphere accessory with a 450 W Xenon lamp as the excitation source, attached to a "NanoLog" spectrofluorometer (Horiba Jobin Yvon). The same instrument was also used to measure the fluorescence lifetime with NanoLED-260 and NanoLED-340, respectively, as excitation light sources (λ = 266 nm, pulse duration < 1.2 ns; and λ = 332 nm, pulse duration < 1.2 ns). The obtained lifetime curves were fitted by DAS6 v6.5 Software.

4.4. Quantum chemical calculations

The optical, structural and vibrational properties of boron nitride were investigated using density functional theory (DFT). A cluster-based approach consisting of 180 atoms arranged in 61 rings was employed to interpret the experimental data of BNDs. All of the calculations were performed using the Gaussian 16 code [52]. *h*-BN clusters have been firstly optimized and the corresponding energies and vibrational modes calculated within density functional theory

(DFT) by using B3PW91 (Becke exchange, Perdew and Wang correlation) functional [53]. The basis sets for B, N, and H were 6-31G(d,p). The electronic excitation energies were calculated based on the time-dependent (TD)-DFT method within density functional theory (DFT) with Becke's three parameters and the Lee−Yang−Parr's nonlocal correlation functional (B3LYP) starting from the relaxed structures [54, 55]. The calculations were performed using vacuum as the medium. GaussView 6 was used to interpret the computed data [56]. Vibration frequencies were rescaled by a factor of 0.9501 [53].

Declaration of Competing Interest

The authors do not have any financial/commercial conflict of interest.

Appendix A. Supplementary material

Supplementary data to this article can be found online at *https://doi.org/10.1016/j.jcis.XXX*.

References

[1] C.R. Dean, A.F. Young, I. Meric, C. Lee, L. Wang, S. Sorgenfrei, K. Watanabe, T. Taniguchi, P. Kim, K.L. Shepard, J. Hone, Boron nitride substrates for high-quality graphene electronics, Nat. Nanotechnol. 5 (2010) 722-726. *https://doi.org/10.1038/nnano.2010.172*.

[2] K. Watanabe, T. Taniguchi, H. Kanda, Direct-bandgap properties and evidence for ultraviolet lasing of hexagonal boron nitride single crystal, Nat. Mater. 3 (2004) 404-409. *https://doi.org/10.1038/nmat1134*.

[3] J.D. Caldwell, I. Aharonovich, G. Cassabois, J.H. Edgar, B. Gil, D.N. Basov, Photonics with hexagonal boron nitride, Nat. Rev. Mater. 4 (2019) 552-567. *https://doi.org/10.1038/s41578-019-0124-1*.

[4] E. Cannuccia, B. Monserrat, C. Attaccalite, Theory of phonon-assisted luminescence in solids: Application to hexagonal boron nitride, Phys. Rev. B 99 (2019) 081109. *https://doi.org/10.1103/physrevb.99.081109*.

[5] J. Ren, L. Stagi, P. Innocenzi, Hydroxylated boron nitride materials: from structures to functional applications, J. Mater. Sci. 56 (2020) 4053–4079. *https://doi.org/10.1007/s10853-020-05513-6*.

[6] Y. Han, Y. Niu, M. Liu, F. Niu, Y. Xu, A rational strategy to develop a boron nitride quantum dot-based molecular logic gate and fluorescent assay of alkaline phosphatase activity, J. Mater. Chem. B 7 (2019) 897-902. *https://10.1039/c8tb02948b*.

[7] L. Stagi, J. Ren, P. Innocenzi, From 2-D to 0-D boron nitride materials, the next challenge, Materials 12 (2019) 3905. *https://doi.org/10.3390/ma12233905*.

[8] J. Ren, L. Stagi, C.M. Carbonaro, L. Malfatti, M.F. Casula, P.C. Ricci, A.E. Del Rio Castillo,

F. Bonaccorso, L. Calvillo, G. Granozzi, P. Innocenzi, Defect-assisted photoluminescence in hexagonal boron nitride nanosheets, 2D Mater. 7 (2020) 045023. *https://doi.org/10.1088/2053-1583/ababf0.*

[9] B. Liu, S. Yan, Z. Song, M. Liu, X. Ji, W. Yang, J. Liu, One-step synthesis of boron nitride quantum dots: Simple chemistry meets delicate nanotechnology, Chem. Eur. J. 22 (2016) 18899-18907. *https://doi.org/10.1002/chem.201603935.*

[10] B. Huo, B. Liu, T. Chen, L. Cui, G. Xu, M. Liu, J. Liu, One-step synthesis of fluorescent boron nitride quantum dots via a hydrothermal strategy using melamine as nitrogen source for the detection of ferric ions, Langmuir 33 (2017) 10673-10678. *https://doi.org/10.1021/acs.langmuir.7b01699.*

[11] A. Kainthola, K. Bijalwan, S. Negi, H. Sharma, C. Dwivedi, Hydrothermal synthesis of highly stable boron nitride nanoparticles, Mater. Today Proc. 28 (2020) 138-140. *https://doi.org/10.1016/j.matpr.2020.01.452.*

[12] J. Ren, L. Malfatti, S. Enzo, C.M. Carbonaro, L. Calvillo, G. Granozzi, P. Innocenzi, Boron oxynitride two-colour fluorescent dots and their incorporation in a hybrid organic-inorganic film, J. Colloid Interface Sci. 560 (2020) 398-406. *https://doi.org/10.1016/j.jcis.2019.10.020.*

[13] Z. Lei, S. Xu, J. Wan, P. Wu, Facile preparation and multifunctional applications of boron nitride quantum dots, Nanoscale 7 (2015) 18902-18907. *https://doi.org/10.1039/c5nr05960g.*

[14] M. Liu, Y. Xu, Y. Wang, X. Chen, X. Ji, F. Niu, Z. Song, J. Liu, Boron nitride quantum dots with solvent-regulated blue/green photoluminescence and electrochemiluminescent behavior for versatile applications, Adv. Opt. Mater. 5 (2017) 1600661. *https://doi.org/10.1002/adom.201600661.*

[15] L. Fan, Y. Zhou, M. He, Y. Tong, X. Zhong, J. Fang, X. Bu, Facile microwave approach to controllable boron nitride quantum dots, J. Mater. Sci. 52 (2017) 13522-13532. *https://doi.org/10.1007/s10853-017-1395-9.*

[16] S. Angizi, A. Hatamie, H. Ghanbari, A. Simchi, Mechanochemical green synthesis of exfoliated edge-functionalized boron nitride quantum dots: Application to vitamin c sensing through hybridization with gold electrodes, ACS Appl. Mater. Interfaces 10 (2018) 28819-28827. *https://doi.org/10.1021/acsami.8b07332.*

[17] M. Mackoit-Sinkevičienė, M. Maciaszek, C.G.V.d. Walle, A. Alkauskas, Carbon dimer defect as a source of the 4.1 eV luminescence in hexagonal boron nitride, Appl. Phys. Lett. 115 (2019) 212101. *https://doi.org/10.1063/1.5124153.*

[18] N. Mendelson, D. Chugh, J.R. Reimers, T.S. Cheng, A. Gottscholl, H. Long, C.J. Mellor, A. Zettl, V. Dyakonov, P.H. Beton, Identifying carbon as the source of visible single-photon emission from hexagonal boron nitride, Nat. Mater. (2020). *https://doi.org/10.1038/s41563-020-00850-y.*

[19] V. Kumar, K. Nikhil, P. Roy, D. Lahiri, I. Lahiri, Emergence of fluorescence in boron nitride nanoflakes and its application in bioimaging, RSC Adv. 6 (2016) 48025-48032. *https://doi.org/10.1039/c6ra05288f.*

[20] S. Umrao, A.K. Maurya, V. Shukla, A. Grigoriev, R. Ahuja, M. Vinayak, R.R. Srivastava, P.S. Saxena, I.K. Oh, A. Srivastava, Anticarcinogenic activity of blue fluorescent hexagonal boron nitride quantum dots: as an effective enhancer for DNA cleavage activity

of anticancer drug doxorubicin, Mater. Today Bio 1 (2019) 100001. *https://doi.org/10.1016/j.mtbio.2019.01.001*.

[21] T. Sainsbury, A. Satti, P. May, Z. Wang, I. McGovern, Y.K. Gun'ko, J. Coleman, Oxygen radical functionalization of boron nitride nanosheets, J. Am. Chem. Soc. 134 (2012) 18758-18771. *https://doi.org/10.1021/ja3080665*.

[22] Q. Cai, D. Scullion, A. Falin, K. Watanabe, T. Taniguchi, Y. Chen, E.J.G. Santos, L.H. Li, Raman signature and phonon dispersion of atomically thin boron nitride, Nanoscale 9 (2017) 3059-3067. *https://doi.org/10.1039/c6nr09312d*.

[23] R.V. Gorbachev, I. Riaz, R.R. Nair, R. Jalil, L. Britnell, B.D. Belle, E.W. Hill, K.S. Novoselov, K. Watanabe, T. Taniguchi, A.K. Geim, P. Blake, Hunting for monolayer boron nitride: Optical and raman signatures, Small 7 (2011) 465-468. *https://doi.org/10.1002/smll.201001628*.

[24] J. Ren, L. Stagi, L. Malfatti, S. Garroni, S. Enzo, P. Innocenzi, Boron nitride–titania mesoporous film heterostructures, Langmuir (2021). *https://doi.org/10.1021/acs.langmuir.1c00460*.

[25] L. Museur, E. Feldbach, A. Kanaev, Defect-related photoluminescence of hexagonal boron nitride, Phys. Rev. B 78 (2008) 155204. *https://doi.org/10.1103/physrevb.78.155204*.

[26] T.Q.P. Vuong, G. Cassabois, P. Valvin, E. Rousseau, A. Summerfield, C.J. Mellor, Y. Cho, T.S. Cheng, J.D. Albar, L. Eaves, C.T. Foxon, P.H. Beton, S.V. Novikov, B. Gil, Deep ultraviolet emission in hexagonal boron nitride grown by high-temperature molecular beam epitaxy, 2D Mater. 4 (2017) 021023. *https://doi.org/10.1088/2053-1583/aa604a*.

[27] H. Hamdi, G. Thiering, Z. Bodrog, V. Ivády, A. Gali, Stone–Wales defects in hexagonal boron nitride as ultraviolet emitters, NPJ Comput. Mater. 6 (2020) 178. *https://doi.org/10.1038/s41524-020-00451-y*.

[28] G. Cassabois, P. Valvin, B. Gil, Hexagonal boron nitride is an indirect bandgap semiconductor, Nat. Photonics 10 (2016) 262-266. *https://doi.org/10.1038/nphoton.2015.277*.

[29] J. Tauc, Optical properties and electronic structure of amorphous Ge and Si, Mater. Res. Bull. 3 (1968) 37-46. *https://doi.org/10.1016/0025-5408(68)90023-8*.

[30] S.H. Lee, H. Jeong, O.F.N. Okello, S. Xiao, S. Moon, D.Y. Kim, G.-Y. Kim, J.-I. Lo, Y.-C. Peng, B.-M. Cheng, H. Miyake, S.-Y. Choi, J.K. Kim, Improvements in structural and optical properties of wafer-scale hexagonal boron nitride film by post-growth annealing, Sci. Rep. 9 (2019) 10590. *https://doi.org/10.1038/s41598-019-47093-9*.

[31] R.S. Singh, R.Y. Tay, W.L. Chow, S.H. Tsang, G. Mallick, E.H.T. Teo, Band gap effects of hexagonal boron nitride using oxygen plasma, Appl. Phys. Lett. 104 (2014) 163101. *https://doi.org/10.1063/1.4872318*.

[32] R. Geick, C.H. Perry, G. Rupprecht, Normal modes in hexagonal boron nitride, Phys. Rev. 146 (1966) 543-547. *https://doi.org/10.1103/physrev.146.543*.

[33] Y. Wang, Z. Shi, J. Yin, Boron nitride nanosheets: large-scale exfoliation in methanesulfonic acid and their composites with polybenzimidazole, J. Mater. Chem. 21 (2011) 11371-11377. *https://doi.org/10.1039/c1jm10342c*.

[34] W. Cai, N. Hong, X. Feng, W. Zeng, Y. Shi, Y. Zhang, B. Wang, Y. Hu, A facile strategy to simultaneously exfoliate and functionalize boron nitride nanosheets via Lewis acid-base interaction, Chem. Eng. J 330 (2017) 309-321. *https://doi.org/10.1016/j.cej.2017.07.162*.

[35] D. Kong, D. Zhang, H. Guo, J. Zhao, Z. Wang, H. Hu, J. Xu, C. Fu, Functionalized boron nitride nanosheets/poly (L-lactide) nanocomposites and their crystallization behavior, Polymers 11 (2019) 440. *https://doi.org/10.3390/polym11030440*.

[36] S. Zhou, T. Xu, F. Jiang, N. Song, L. Shi, P. Ding, High thermal conductivity property of polyamide-imide/boron nitride composite films by doping boron nitride quantum dots, J. Mater. Chem. C 7 (2019) 13896-13903. *10.1039/C9TC04381K*.

[37] Y. Zhan, J. Yang, L. Guo, F. Luo, B. Qiu, G. Hong, Z. Lin, Targets regulated formation of boron nitride quantum dots – Gold nanoparticles nanocomposites for ultrasensitive detection of acetylcholinesterase activity and its inhibitors, Sens. Actuators B Chem. 279 (2019) 61-68. *https://doi.org/10.1016/j.snb.2018.09.097*.

[38] A.S. Rocha, G.C. Costa, L.R.R. de Araujo, W.A. Misael, R.R. Oliveira, A.B. Rocha, Insights into the phosphate species on niobia treated with H_3PO_4, Catal. Lett. 150 (2020) 1496-1504. *https://doi.org/10.1007/s10562-019-03056-3*.

[39] W.W. Rudolph, Raman- and infrared-spectroscopic investigations of dilute aqueous phosphoric acid solutions, Dalton Trans. 39 (2010) 9642-9653. *https://doi.org/10.1039/c0dt00417k*.

[40] H.-R. Zhao, J.-H. Ding, H.-B. Yu, Phosphorylated boron nitride nanosheets as highly effective barrier property enhancers, Ind. Eng. Chem. Res. 57 (2018) 14096-14105. *https://doi.org/10.1021/acs.iecr.8b03220*.

[41] N.I. Kovtyukhova, Y. Wang, R. Lv, M. Terrones, V.H. Crespi, T.E. Mallouk, Reversible intercalation of hexagonal boron nitride with brønsted acids, J. Am. Chem. Soc. 135 (2013) 8372-8381. *https://doi.org/doi.org/10.1021/ja403197h*.

[42] Q. Lu, Q. Zhao, T. Yang, C. Zhai, D. Wang, M. Zhang, Preparation of boron nitride nanoparticles with oxygen doping and a study of their room-temperature ferromagnetism, ACS Appl. Mater. Interfaces 10 (2018) 12947-12953. *https://doi.org/doi.org/10.1021/acsami.7b17932*.

[43] L. Lin, Y. Xu, S. Zhang, I.M. Ross, A.C.M. Ong, D.A. Allwood, Fabrication and Luminescence of Monolayered Boron Nitride Quantum Dots, Small 10 (2014) 60-65. *https://doi.org/10.1002/smll.201301001*.

[44] K. Yang, P. Jia, J. Hou, T. Bu, X. Sun, Y. Liu, L. Wang, Innovative dual-emitting ratiometric fluorescence sensor for tetracyclines detection based on boron nitride quantum dots and europium ions, ACS Sustain. Chem. Eng. 8 (2020) 17185-17193. *https://doi.org/10.1021/acssuschemeng.0c05872*.

[45] J.-H. Jung, M. Kotal, M.-H. Jang, J. Lee, Y.-H. Cho, W.-J. Kim, I.-K. Oh, Defect engineering route to boron nitride quantum dots and edge-hydroxylated functionalization for bio-imaging, RSC Adv. 6 (2016) 73939-73946. *https://doi.org/10.1039/C6RA12455K*.

[46] S. Hong, C.-S. Lee, M.-H. Lee, Y. Lee, K.Y. Ma, G. Kim, S.I. Yoon, K. Ihm, K.-J. Kim, T.J. Shin, S.W. Kim, E.-c. Jeon, H. Jeon, J.-Y. Kim, H.-I. Lee, Z. Lee, A. Antidormi, S. Roche, M. Chhowalla, H.-J. Shin, H.S. Shin, Ultralow-dielectric-constant amorphous boron nitride, Nature 582 (2020) 511-514. *https://doi.org/10.1038/s41586-020-2375-9*.

[47] K. Jasuja, K. Ayinde, C.L. Wilson, S.K. Behura, M.A. Ikenbbery, D. Moore, K. Hohn, V. Berry, Introduction of protonated sites on exfoliated, large-area sheets of hexagonal boron nitride, ACS Nano 12 (2018) 9931-9939. *https://doi.org/10.1021/acsnano.8b03651*.

[48] S. Angizi, F. Shayeganfar, M.H. Azar, A. Simchi, Surface/edge functionalized boron

nitride quantum dots: Spectroscopic fingerprint of bandgap modification by chemical functionalization, Ceram. Int. 46 (2020) 978-985. *https://doi.org/10.1016/j.ceramint.2019.09.061.*

[49] C.-K. Lin, Theoretical study of nitrogen-doped graphene nanoflakes: Stability and spectroscopy depending on dopant types and flake sizes, J. Comput. Chem. 39 (2018) 1387-1397. *https://doi.org/10.1002/jcc.25206.*

[50] C. Elias, P. Valvin, T. Pelini, A. Summerfield, C.J. Mellor, T.S. Cheng, L. Eaves, C.T. Foxon, P.H. Beton, S.V. Novikov, B. Gil, G. Cassabois, Direct band-gap crossover in epitaxial monolayer boron nitride, Nat. Commun. 10 (2019) 2639. *https://doi.org/10.1038/s41467-019-10610-5.*

[51] P. Valerius, C. Herbig, M. Will, M.A. Arman, J. Knudsen, V. Caciuc, N. Atodiresei, T. Michely, Annealing of ion-irradiated hexagonal boron nitride on Ir(111), Phys. Rev. B 96 (2017) 235410. *https://doi.org/10.1103/physrevb.96.235410.*

[52] M.J. Frisch, G.W. Trucks, H.B. Schlegel, G.E. Scuseria, M.A. Robb, J.R. Cheeseman, G. Scalmani, V. Barone, G.A. Petersson, H. Nakatsuji, X. Li, M. Caricato, A.V. Marenich, J. Bloino, B.G. Janesko, R. Gomperts, B. Mennucci, H.P. Hratchian, J.V. Ortiz, A.F. Izmaylov, J.L. Sonnenberg, Williams, F. Ding, F. Lipparini, F. Egidi, J. Goings, B. Peng, A. Petrone, T. Henderson, D. Ranasinghe, V.G. Zakrzewski, J. Gao, N. Rega, G. Zheng, W. Liang, M. Hada, M. Ehara, K. Toyota, R. Fukuda, J. Hasegawa, M. Ishida, T. Nakajima, Y. Honda, O. Kitao, H. Nakai, T. Vreven, K. Throssell, J.A. Montgomery Jr., J.E. Peralta, F. Ogliaro, M.J. Bearpark, J.J. Heyd, E.N. Brothers, K.N. Kudin, V.N. Staroverov, T.A. Keith, R. Kobayashi, J. Normand, K. Raghavachari, A.P. Rendell, J.C. Burant, S.S. Iyengar, J. Tomasi, M. Cossi, J.M. Millam, M. Klene, C. Adamo, R. Cammi, J.W. Ochterski, R.L. Martin, K. Morokuma, O. Farkas, J.B. Foresman, D.J. Fox, Gaussian 16 Rev. C.01, Wallingford, CT, 2016.

[53] M.A. Palafox, DFT computations on vibrational spectra: Scaling procedures to improve the wavenumbers, Phys. Sci. Rev. 3 (2018). *https://doi.org/10.1515/psr-2017-0184.*

[54] A.D. Becke, Density-functional thermochemistry. III. The role of exact exchange, J. Chem. Phys. 98 (1993) 5648-5652. *https://doi.org/10.1063/1.464913.*

[55] C. Lee, W. Yang, R.G. Parr, Development of the Colle-Salvetti correlation-energy formula into a functional of the electron density, Phys. Rev. B 37 (1988) 785-789. *https://doi.org/10.1103/physrevb.37.785.*

[56] R. Dennington, T.A. Keith, J.M. Millam, GaussView, Version 6.1, Semichem Inc. Shawnee Mission, KS, 2016.